ACS APPLIED MATERIALS & INTERFACES

Research Article

Cite This: ACS Appl. Mater. Interfaces 2018, 10, 43219−43229

www.acsami.org

From Alloy to Oxide: Capturing the Early Stages of Oxidation on Ni−Cr(100) Alloys

William H. Blades and Petra Reinke*

Department of Materials Science and Engineering, University of Virginia, Charlottesville, Virginia 22904, United States

Supporting Information

ABSTRACT: The interaction of oxygen with Ni−Cr(100) alloy surfaces is studied using scanning tunneling microscopy (STM) and spectroscopy (STS) to observe the initial steps of oxidation and formation of the alloy−oxide interface. The progression of oxidation was observed for Ni(100) and Ni−Cr(100) thin films including Ni−8 wt % Cr(100) and Ni−12 wt % Cr(100), which were grown on MgO(100) in situ. These surfaces were exposed to between 1 and 150 L O_2 at 500 °C, and additional annealing steps were performed at 500 and 600 °C. Each oxidation and annealing step was studied with STM and STS, and differential conductance maps delivered spatially resolved information on doping and band gap distributions. Initial NiO nucleation and growth begins along the step edges of the Ni−Cr alloy accompanied by the formation of small oxide particles on the terraces. The incubation period known in oxidation of Ni(100) is absent on Ni−Cr alloy surfaces illustrating the significant changes in surface chemistry triggered by Cr-alloying. Step edge faceting is initiated by oxide decoration along the step edges and is expressed as moiré patterns in the STM images. The surface oxide can be characterized by NiONi(6 × 7) and NiO−Ni(7 × 8) coincidence lattices, which have a cube-on-cube epitaxial relationship. Small patches of NiO are susceptible to reduction during annealing; however, additional oxide coverage stabilizes the NiO. NiO regions are interspersed with areas covered predominantly with a novel cross-type reconstruction, which is interpreted tentatively as a Cr-rich, phase-separated region. Statistical analysis of the geometric features of the surface oxide including step edge heights, and NiO wedge angles illustrates the layer-by-layer growth mode of NiO in this pre-Cabrera−Mott regime, and the restructuring of the alloy−oxide interface during the oxidation process. This experimental approach has offered greater insight into the progression of oxide growth in Ni−Cr thin films and underscores the dramatic impact of alloying on oxidation process in the pre-Cabrera−Mott regime.

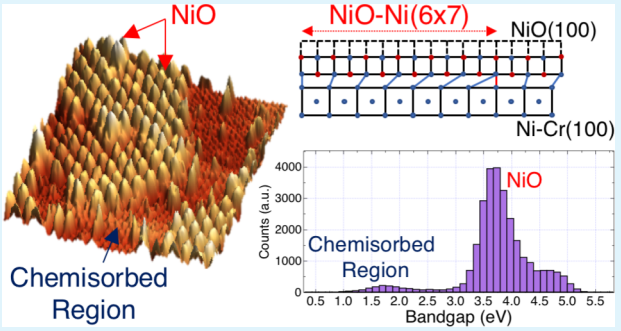

KEYWORDS: *Ni−Cr alloy, oxidation, NiO, coincidence lattice, scanning tunneling microscopy, scanning tunneling spectroscopy, surface reactivity*

INTRODUCTION

The complex processes that govern the reactions of molecular oxygen and corrosive solutions with transition metal alloys are of high technical relevance and have garnered significant interest for many decades.[1−9] The economic cost of materials breakdown due to corrosion and oxidation is staggering, and hence corrosion resistance is an important design parameter for technical alloys. The study of corrosion processes, including dry as well as aqueous corrosion reactions, is motivated by the need to reduce the overall economic burden incurred by materials degradation. A large body of work exists on performance, passivation, and breakdown of the oxide layers, but attention has turned only recently to the initial steps in alloy oxidation and, most importantly, formation of the alloy−oxide interface.[1,7,9−11] These initial reactions bias the continued growth of the protective oxide scale and therefore critically influence its passivity and performance. A mechanistic understanding of initial reactions steps and the formation of the alloy−oxide interface is therefore indispensable to future alloy design.

The initial reaction steps are complex, and synergistic interactions between the alloying elements and oxygen are at the heart of understanding the alloy-to-oxide transformation. Our work targets Ni−Cr alloys, which possess excellent mechanical properties and high degree of corrosion resistance, and have practical application in an array of industrial and military systems. The structure and composition of the oxide layer, which includes Ni- and Cr-oxides, are highly sensitive to composition, temperature, and crystallographic orientation.[12−14] A deeper understanding of the relationship between initial oxide formation, oxide growth, and properties is therefore important to engineer passive layers and future alloys.

To study the subtleties that govern the initial nucleation and growth of surface oxides, scanning tunneling microscopy/spectroscopy (STM/STS) is employed to gain insight into the evolution of oxide layers on Ni(100) and Ni−Cr(100) thin-

Received: September 2, 2018
Accepted: November 19, 2018
Published: November 19, 2018

Downloaded via NORTHWESTERN UNIV on March 28, 2019 at 20:37:13 (UTC).
See https://pubs.acs.org/sharingguidelines for options on how to legitimately share published articles.

© 2018 American Chemical Society

DOI: 10.1021/acsami.8b15210
ACS Appl. Mater. Interfaces 2018, 10, 43219−43229

film surfaces as they are exposed to O_2.[1,2] The work presented in this article covers temperatures of 500 and 600 °C where the competition between Ni- and Cr-oxide formation is significant, and high-quality extended crystalline layers and interfaces are formed. In contrast, recent work modeled the oxidation of Ni−Cr(100) at 300 °C, a relatively low temperature where Cr-supply from the bulk is severely limited, and short-range surface diffusion controls oxidation.[11]

Cabrera−Mott and Wagner's theory are models that are frequently used as the basis to describe the growth of oxide layers, and are suitable to understand the growth kinetics of oxide layers across different length scales.[1,16−18] Cabrera−Mott theory is applied to describe the growth kinetics of oxide layers that range from about 1 to 10 nm in thickness. The growth of the oxide film is dominated by ion transport through the layer, which is driven by the electric field between the oxide−metal and gas phase/adsorbate−oxide interfaces. This interaction controls oxide growth until a limiting thickness is reached, and the electric field is diminished.[1,16,18] Once the oxide reaches this limiting thickness, Wagner's theory, which assumes a net charge neutral diffusion of ions and a field arising via ambipolar diffusion through the oxide, is suited to understand the growth rate.[19] Both of these models assume that film growth is planar and homogeneous across the surface; however, the initial stages of growth before a complete oxide layer is formed are not fully understood. To this end, the present study specifically considers the transition from alloy to oxide during a growth regime prior to the Cabrera−Mott regime tentatively termed the "pre-Cabrera−Mott regime", by capturing the initial stages of Ni(100) and Ni−Cr(100) thin-film oxidation. Our report aims to gain a better understanding of the oxidation pathways for Ni(100), Ni−8 wt % Cr(100), and Ni−12 wt % Cr(100) at temperatures of 500−600 °C, and the formation of the alloy−oxide interface.

The oxidation of Ni−Cr alloys is governed by the competing formation of NiO, Cr_2O_3, and mixed oxides such as $NiCr_2O_4$. Temperature, alloy composition, crystallographic orientation, and partial pressure of oxygen all influence the reaction pathways and consequently the oxide products.[1,6,7,13,14,20−25] In general, the oxidation of Ni−Cr below 700 °C, and for alloys with less than 20 wt % Cr, begins with the formation of NiO, which is generally attributed to the lower activation barrier for nucleation on a cube-on-cube epitaxy for the rock-salt structure. NiO therefore dominates the initial oxide layer, and Cr_2O_3 subsequently forms at the alloy−oxide interface by internal oxidation.[1−3,26] A consequence of this reaction sequence is a layered oxide structure. A limited supply of Cr in the Cr-poorer alloys impedes the formation of a continuous Cr_2O_3 layer thus diminishing the oxide's protective function.

In this work we use Ni(100) and Ni−Cr(100) alloy surfaces as model systems. The oxidation of Ni(100) itself is a rather peculiar process: dissociative chemisorption of O_2 leads to the formation of p(2 × 2)O and then c(2 × 2)O reconstructions which are followed at room temperature by the nucleation of oxide at the step edges.[27−31] However, at elevated temperatures the formation of NiO is delayed, and increasingly large oxygen exposures are required for its nucleation. Following the work by Kopatzki et al.[27] the incubation period can be attributed to the loss of preferential nucleation sites at the step edges due to faceting into {100} segments, which is driven by the reconstruction and achieved by the increased adatom mobility at higher temperatures. The NiO nucleation on Ni(100) relies on the availability of step edge nucleation sites, while nucleation on the terrace is suppressed. As a consequence, the Ni(100) surface requires relatively large doses of O_2 to initiate oxide formation.[27−29,32]

The oxidation of Cr(100) progresses via a Cr(100)−c(2 × 4)O chemisorbed structure followed by the formation of Cr_2O_3 when the Cr surface is oxidized and subsequently annealed.[33−37] Oxidation of Cr(100) at room temperature starts with the formation of p(1 × 1)O ad-layers, where the O atoms are incorporated into in the 4-fold-site on the Cr(100) bcc lattice. This ad-layer is accompanied by small domains of a $(\sqrt{5} \times \sqrt{5})R27°$ subsurface vacancy structure showing at most short-range ordering of vacancies and not the long-range ordering of missing row reconstructions.[37] The p(1 × 1)O surface is structurally identical to a single layer of CrO, a surface stabilized oxide with NaCl structure where the O atoms are fully integrated in the top metal layer. It is still unclear how the transformation from the CrO layer into the Cr_2O_3 oxide is achieved at the atomic scale. In contrast, Cr-atoms in Ni−Cr are embedded in an fcc bonding environment further complicating comparisons to the pure elements. The different reaction pathways between Ni(100) and Cr(100) surfaces raise the expectation that alloying results in a unique oxidation process that differs from the pure metals.

In a recent study we followed the initial steps in the oxidation of a Ni−5 wt % Cr(100) thin film at temperatures of 300 °C, which is in the regime of very limited bulk Cr-diffusivity.[11] This is a relatively low temperature for Ni−Cr oxidation and, in contrast to the present study performed at 500 and 600 °C, did not yield a high-quality crystalline oxide layer. The oxide islands grew to a critical height, propagated laterally, and eventually formed a near complete oxide layer. The initial growth of the surface oxide islands was shown to be controlled by short-range oxygen diffusion and was modeled using a screening length of only a few nanometers, which suggests that growth and coalescence are localized to the edge of the oxide island.

The work presented here focuses on the comparison between Ni(100), Ni−8 wt % Cr(100), and Ni−12 wt % Cr(100) oxidation at 500 °C using Ni−Cr(100) thin films grown under ultrahigh vacuum conditions on MgO(100).[38] These alloy compositions and oxidation conditions favor NiO formation, and enable us to isolate the impact of Cr on the surface reactions within the pre-Cabrera−Mott regime. The evolution of surface oxides, and the alloy−oxide interface is measured using STM and STS, which deliver the geometric and electronic structure of the surface. We present a detailed analysis of the NiO−alloy interface and the evolution of surface oxides on Ni−Cr(100), and use STS to capture local variations in electronic structure and doping. The oxidation of this binary alloy relies on the intricate interplay between the chemistry of two highly reactive elements. The study of unique and often synergistic reaction pathways, as well as the geometric and electronic properties of ultrathin oxides and interfaces, will contribute to understanding how to improve the quality of passive layers on alloy surfaces.

EXPERIMENTAL METHODS

The oxidation experiments were conducted under ultrahigh vacuum (UHV) conditions using an Omicron Nanotechnology variable temperature scanning probe microscopy (VT-SPM) system. A tungsten tip was prepared electrochemically and used for all experiments discussed herein. The base pressure was 2.5×10^{-10} mbar, and imaging was done at ambient temperature. All metal thin

DOI: 10.1021/acsami.8b15210
ACS Appl. Mater. Interfaces 2018, 10, 43219−43229

Table 1. Summary of Oxidation and Annealing Steps[a] for All Alloys

alloy composition	oxidation E_n, annealing A_n	T [°C]	$p(O_2)$ [mbar]	cumulative exposure [L] (individual exposure step)
(i) Ni(100)	E_1	500 °C	2.0×10^{-8} mbar	50 L (+50 L)
	E_2	500 °C	6.0×10^{-8} mbar	200 L (+150 L)
	E_3	500 °C	9.0×10^{-8} mbar	500 L (+300 L)
(ii) Ni−8 wt % Cr	E_1	500 °C	2.0×10^{-9} mbar	1 L
	E_2	500 °C	1.0×10^{-8} mbar	10 L (+9 L)
	E_3	500 °C	5.9×10^{-9} mbar	15 L (+5 L)
(iii) Ni−12 wt % Cr	E_1	500 °C	8.6×10^{-9} mbar	7 L (+7 L)
	A_1	600 °C		annealed 1800 s
	E_2	500 °C	8.6×10^{-9} mbar	14 L (+7 L)
	A_2	500 °C		annealed 1320 s
	A_3	600 °C		annealed 1320 s
	A_4	600 °C		annealed 5400 s

[a]All experiment and processing steps for a given alloy were completed within 24 h of alloy deposition.

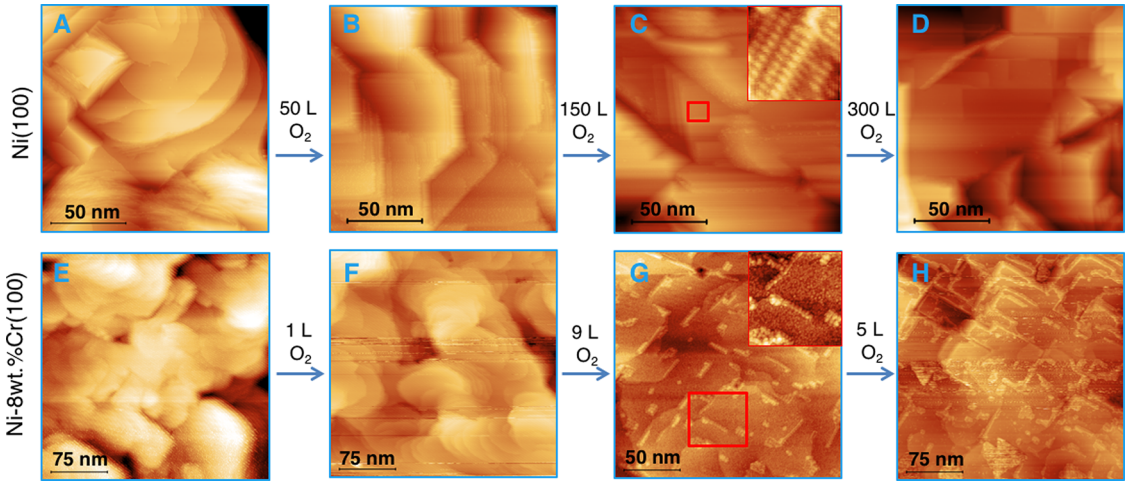

Figure 1. Topography images showing the progression of oxidation for Ni(100) (A−D), and Ni−8 wt % Cr(100) (E−H). The oxidation and annealing steps are indicated in the figure, and summarized in Table 1. The image insets in parts C and G are 14 × 14 and 50 × 50 nm^2, respectively. The oxidation steps were all performed at 500 °C, and imaging conditions are U_{bias} = 2.0 V and I_t = 0.1 nA for all images in this series, except parts A, E, and F which were taken at U_{bias} = 0.15 V and I_t = 0.5 nA.

films were deposited on MgO(100) single crystal substrates that had undergone pretreatment outlined in ref 38. Ni (Alfa Aesar 99.999% purity) and Cr (American Elements, 99.95% purity) were deposited on these MgO(100) substrates by electron beam evaporation using a Mantis EV mini e-beam quad-source. The deposition rates of Ni and Cr were measured using a quartz crystal monitor to accurately adjust the film composition. The deposition of Ni and Ni−Cr thin films followed the procedure developed previously.[38] The Ni−8 wt % Cr(100) and Ni−12 wt % Cr(100) alloys were deposited at a substrate temperature of 400 °C. The composition of the Ni−Cr thin films was verified ex situ, after experimentation, by energy dispersive spectroscopy (EDS) with a Quanta LV650 scanning electron microscope (SEM). Oxygen was introduced through a sapphire leak valve, and all oxidation experiments were performed at 500 °C to form a crystalline oxide layer. The Ni(100) and Ni−Cr(100) surfaces were imaged immediately after deposition, and then after all oxidation and annealing steps as summarized in Table 1. STM and STS were employed to gain insight into the surface topography and local density of states (LDOS) for all deposition and reaction steps. The spectra were recorded by measuring an I/V curve for every third image pixel with an open feedback loop, while topography information was recorded for the next two image pixels with a closed feedback loop set to a tunneling current of 0.1 nA and a bias voltage of 3.0 V. A voltage range of ±3.0 V was used for the STS spectra.

The data from the STS measurements were formatted into density of state and band gap maps using a MATLAB code. This was accomplished by numerically differentiating the I/V curves to generate dI/dV curves. These were then normalized by I/V and expressed as $(dI/dV)/(I/V)$ curves following the procedure described by Feenstra et al.[39,40] Once normalized, the band gap of each curve was numerically determined by calculating the region where $(dI/dV)/(I/V)$ is smaller than a threshold value, i.e., where the DOS is very close to zero. This approach was particularly well-suited for the analysis of a large number of data points. The distributions of valence/conduction band extrema and band gap values were generated from these data. The tangent method for determining the band gap, which takes into account variations in DOS slope at the band edges, was used when a smaller number of data points was considered and is illustrated in the Supporting Information, section S1. The differences between the two methods were generally very small in this materials system and confirmed the correct use of a threshold value for large data sets. The $(dI/dV)/(I/V)$ spectra were then displayed as spatially resolved DOS and band gap maps, respectively, which allows for a direct comparison between topography and electronic structure. Prior to display and analysis of the topography images, each surface was leveled by mean plane subtraction and planarization. The use of these corrections is illustrated in the Supporting Information, section S2, and only values not skewed by image processing are used in the subsequent analysis of step heights and other geometric features.

DOI: 10.1021/acsami.8b15210
ACS Appl. Mater. Interfaces 2018, 10, 43219−43229

RESULTS

Figure 1 provides a comparison between the oxidation of Ni(100) and Ni−8 wt % Cr(100) surfaces to illustrate the impact of alloying on the oxidation process. Figure 1A shows the as-deposited Ni(100) thin film, which has wide terraces with curved step edges consistent with previous reports in the literature.[36] The first oxidation step, Figure 1B, initiated a surface reconstruction, and the steps faceted into parallel {100} segments. The step edge faceting can be attributed to the dissociative chemisorption of O_2 and formation of a c(2 × 2)O reconstruction on the Ni(100) surface.[27] Pure Ni(100) at very low exposures adopts the p(2 × 2)O reconstruction with O atoms positioned in the 4-fold hollow sites, and with increasing exposure the center hollow site becomes occupied to form the c(2 × 2)O structure. The inset in Figure 1C shows a high-resolution image of the facet which is commensurate with the c(2 × 2)O reconstruction. An average spacing of 0.44 ± 0.05 nm separates the rows in the image inset confirming the c(2 × 2)O unit cell.

Reconstruction-induced step faceting removes reactive kink sites causing the surface to become nearly inert against oxide formation, which has been demonstrated in previous studies.[27] Indeed, no oxide islands are seen in Figure 1C,D even after a 300 L exposure of O_2 and is in stark contrast to the rapid development of oxide on the Ni−Cr alloys. According to the literature an oxygen exposure of at least 1200 L is required to grow NiO at elevated temperatures on Ni(100) surfaces.[28] The activation barrier for oxide nucleation increases significantly on faceted terrace edges compared to step edges with kink sites. The c(2 × 2)O reconstruction-induced step edge faceting is held responsible for the extended induction period toward oxide formation.[27] Our observations of the Ni(100) thin-film surfaces are in agreement with the literature, and the behavior of single crystal surfaces.[27,28,30]

Four dominant types of surface features are observed on the alloy surfaces during oxidation and annealing, and their relative abundance is determined by alloy composition, oxygen exposure, and temperature. The parameter space covered in the present article is summarized in Table 1. Some features can be uniquely attributed to a specific oxide due to characteristic structural or electronic signatures, while details of novel reconstructions are observed but not yet fully understood. The surface features in question are as follows:

(1) NiO in a NiO−NiCr$(6 \times 7)_{terrace}$ or NiO−NiCr$(7 \times 8)_{step}$ coincidence lattices are seen in the STM images as moiré patterns, and appear on the terraces and at step edges, respectively. At higher oxygen exposure NiO extends far onto the terrace, is observed on Ni−8 wt % Cr(100) and Ni−12 wt % Cr(100), and has also been reported for Ni(100) albeit at much higher oxygen exposures.[28]

(2) Nanoscale oxide clusters tend to form early in the oxidation process and are located on the terraces.

(3) Several different oxygen-induced reconstructions are on the alloy surface and are distinct from any reconstructions reported for the pure metal surfaces.

(4) Oxide nodules are several nanometers in width and length, and differ structurally and electronically from the surrounding NiO. The nodules have a relatively large apparent height that is highly dependent on bias voltage. The nodules are tentatively assigned to either Cr_2O_3 or spinel $NiCr_2O_4$ and are only observed on the Ni−12 wt % Cr(100) alloy surface at later oxidation and annealing steps.

The Ni(100) surface reaction is compared to Ni−8 wt % Cr(100) oxidation shown in Figure 1E−H, which illustrates the impact of dilute amounts of Cr-alloying on oxidation. The pristine alloy surfaces consist of relatively large terraces up to several 10 nm in width, and step edges with an average apparent height of 0.17 nm ±0.01—half the unit cell height of Ni (a_{Ni} = 0.35 nm). The modulation of surface morphology as a function of alloy composition is addressed in a previous publication.[38] The introduction of a small amount of oxygen, 1 L at 500 °C, did not induce an observable reaction, while a cumulative exposure of 10 L (1 L + 9 L) in a second oxidation step initiated the formation of oxide islands and nanoscale clusters (Figure 1G). The oxide population is bimodal and consists of small clusters on the terraces and extended oxide segments along the step edges. The step edge oxide is NiO, which forms a coincidence lattice due to the lattice mismatch between Ni and NiO and is expressed as a characteristic moiré pattern in the STM images. The coincidence lattice is discussed in detail later in this article. During the third oxidation step depicted in Figure 1H the majority of the alloy step edges are decorated with oxide (NiO) and display faceting, which is consistent with the highly anisotropic surface free energy of oxides.[27,41] The oxide-induced step edge faceting is reminiscent of the reconstruction-induced faceting for Ni(100). The general evolution of surface features and oxides follows the same trend for the Ni−8 wt % Cr(100) and Ni−12 wt % Cr(100) alloys, although the oxidation is more rapid for the Ni−12 wt % Cr(100) alloy—especially the formation of NiO advances at a faster pace for the same oxygen exposure which is discussed in detail in the next paragraph. The preferential formation of NiO over Cr_2O_3 is in agreement with the work of Luo et al., who documented NiO layer growth on Ni−10 atom % Cr alloys.[6,7]

The Ni−12 wt % Cr(100) alloy was oxidized and annealed in several sequential reaction steps as illustrated in Figure 2 and summarized in Table 1. Figure 2A shows the surface prior to oxidation.[38] The first oxidation step (Figure 2B) corresponds to reaction step E_1 as defined in Table 1, and leads to step edge decoration with NiO, and formation of an abundance of nanoscale clusters on the terraces. This reaction sequence is very similar to the Ni−8 wt % Cr(100) surface, and differs only in the amount of NiO. NiO starts to grow into the flat terrace as the oxygen exposure is increased. Line scans of the oxide on the terrace reveal an average spacing of the maxima of 2.50 ± 0.02 nm commensurate with the NiO−Ni(6 × 7) coincidence lattice along the [100] direction. The step edge oxide shows a more compact pattern with 2.01 ± 0.07 nm spacing measured edge-to-edge with respect to the repeat unit in NiO. This corresponds to NiO−Ni(7 × 8) along the [110] direction in both lattices. The Supporting Information includes a detailed illustration of the measurement directions. The increased NiO coverage in Ni−12 wt % Cr(100) in comparison to Ni−8 wt % Cr(100) shows that NiO nucleation and growth depends sensitively on the Cr content in the alloy.

The almost complete step edge decoration, and extended coverage of the terraces with NiO−NiCr(6 × 7), is seen in the reaction steps E_2, A_2, A_3, and A_4 (Figure 2D), which follow A_1 (Figure 2C). A direct comparison of the surface after A_2, A_3, and A_4 is included in the Supporting Information, Figure S3. Figures 6 and 7 show the surface after E_2. All statistical analysis

DOI: 10.1021/acsami.8b15210
ACS Appl. Mater. Interfaces 2018, 10, 43219−43229

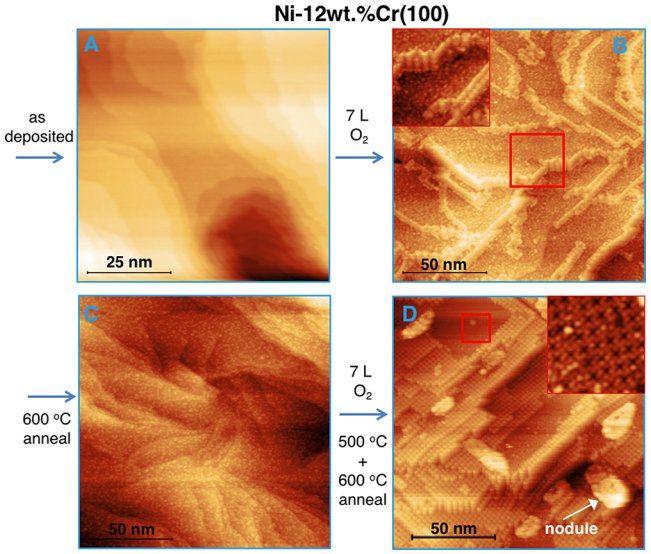

Figure 2. STM images captured for Ni−12 wt % Cr(100): (A) as-deposited alloy surface, (B) after 7 L exposure at 500 °C, and (C) subsequent annealing at 600 °C (A_1 in Table 1). (D) Observed after the final annealing step at 600 °C (A_4 in Table 1). The complete step edge decoration, and extended coverage of the terraces with NiO, is seen in all samples after A_1 corresponding to the reaction steps E_2, A_2, A_3, and A_4. A direct comparison of the surface after A_2, A_3, and A_4 is included in the Supporting Information, Figure S3. Part B includes an inset with a higher-resolution view of the step edge oxide, and part D shows an inset with the cross-type reconstruction. Imaging conditions were U_{bias} = 2.0 V and I_t = 0.1 nA.

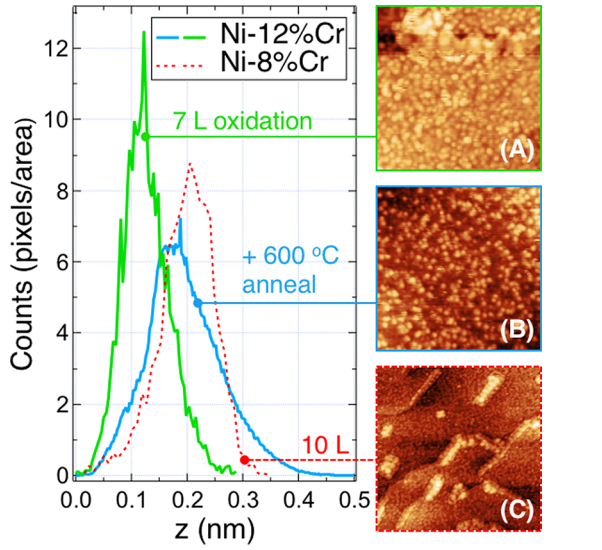

Figure 3. Apparent height distributions of the oxide particles on the terraces for images A−C. Distributions and images are from the Ni−12 wt % Cr(100) sample after (A) 7 L of O_2 exposure and (B) 600 °C anneal. The distribution from image C corresponds to Ni−8 wt % Cr(100) sample after a cumulative exposure of 10 L.

of coincidence lattices on terraces and steps, step heights, their U_{bias} dependent behavior, as well as the electronic characteristics of the different types of surface features has been performed for images recorded after all oxidation and annealing steps. While the abundance of the surface features changes throughout the reaction sequence, their geometric and electronic characteristics remain unchanged. For example, all step edge NiO presents a NiO−Ni(7 × 8) coincidence lattice independent of whether it is observed after reactions step E_1 or E_4 for Ni−12 wt % Cr(100), or E_3 for Ni−8 wt % Cr(100).

In the early oxidation steps the terraces are covered by nanoclusters (Figures 2B and 3), which form a dense layer. The relatively high cluster density precludes a reliable measurement of the lateral size distribution due to tip convolution effects. Distributions of apparent height are therefore used for comparison and measured on 20 × 20 nm^2 areas on the terraces. The height distribution is measured as "apparent height above baseline" over the entire image with identical image sizes for all three oxidation steps. The baseline is defined as the positions with the smallest apparent height in the pockets between the clusters for each terrace individually. The baseline pockets might be the bare alloy, or an alloy with chemisorbed oxygen, and it was not possible to identify their chemical and bonding state unambiguously. The apparent height distributions reveal rather shallow clusters with a maximum around 0.12 and 0.21 nm for Ni−12 wt % Cr(100), and Ni−8 wt % Cr(100), respectively. The poorly defined cluster shape, and relatively large width of distributions, which can stem from variations in topographic height as well as local density of states, is commensurate with suboxides or amorphous oxide with variable composition formed on the surface of the random solid-solution Ni−Cr alloy. The nanocluster height distributions for the two alloys are nearly symmetric in the initial reaction step, although the average cluster height is larger for Ni—8 wt % Cr(100). We attribute this larger apparent height to the higher cumulative oxygen exposure. After the first 600 °C anneal step of Ni−12 wt % Cr(100) the clusters appear to ripen, which is expressed by a shift of the height distribution maximum to larger values and an increasing population at larger height. The STS spectra revealed a band gap for the nanocluster-decorated terrace around 4.0 eV, but the lack of well-defined geometric structure prevents attribution to a specific oxide.

The annealing step A_1 at 600 °C (Ni−12 wt % Cr) leads at the same time to the complete loss of step edge oxides (Figure 2C). The exposed alloy step edges revert to a more curved morphology and are reminiscent of the initial alloy surface shown in Figure 2A. Hence, step edge motion in Ni−Cr alloys is relatively facile, and straight edges are stabilized by NiO. The loss of step edge NiO can be attributed to a chemical reduction due to either the reducing ultrahigh vacuum environment, or a solid-state reaction with Cr where the reaction products (Cr_2O_3 or $NiCr_2O_4$) are integrated in the nanocluster population. Reduction of NiO by either reaction can be facilitated by the abundance of undercoordinated edge sites along the narrow strips of edge-oxide. The solid-state reaction pathway is also known to drive the internal oxidation of Ni−Cr in the later stages of the oxidation process.[1,26]

The second 7 L oxidation step at 500 °C (E_2, cumulative exposure of 14 L) drives a rapid increase in the NiO terrace coverage that now envelops a large part of the surface. At the same time nanoclusters, which previously dominated the terraces, have dissolved. Additional annealing steps at 500 and 600 °C have a negligible impact on the surface structure and only remove kinks in the edges of the NiO layer spreading over the terrace (Supporting Information, section S3). The NiO boundaries often coincide with minima in the moiré pattern (Figure 2D, A_4, final annealing step for Ni−12 wt % Cr) and therefore appear to be the most-stable bonding site.

DOI: 10.1021/acsami.8b15210
ACS Appl. Mater. Interfaces 2018, 10, 43219−43229

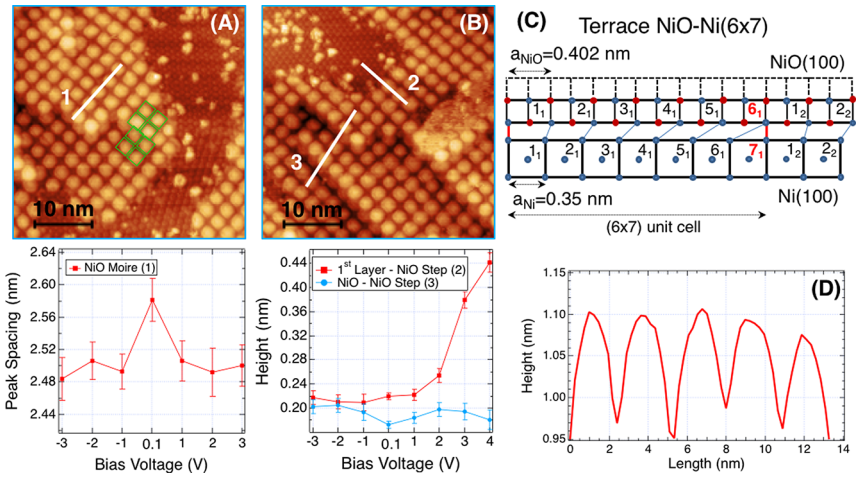

Figure 4. Assessment of the NiO moiré pattern and coincidence lattice measured for Ni−12 wt % Cr(100) after a cumulative oxygen exposure of 14 L and annealing at 500 °C (step A_2 as classified in Table 1). Images A and B were measured at −2.0 V and 0.1 nA. Height and distances were measured at the same image feature, which was recorded at different bias voltages maintaining a feedback current of 0.1 nA. The peak spacing (line 1) is acquired on the NiO moiré pattern; the height distributions are measured across line 2 NiO−NiO, and line 3 NiO-reconstruction. (C) Model of the 6 × 7 NiO−Ni cube-on-cube coincidence lattice. (D) Corresponding line scan along line 1.

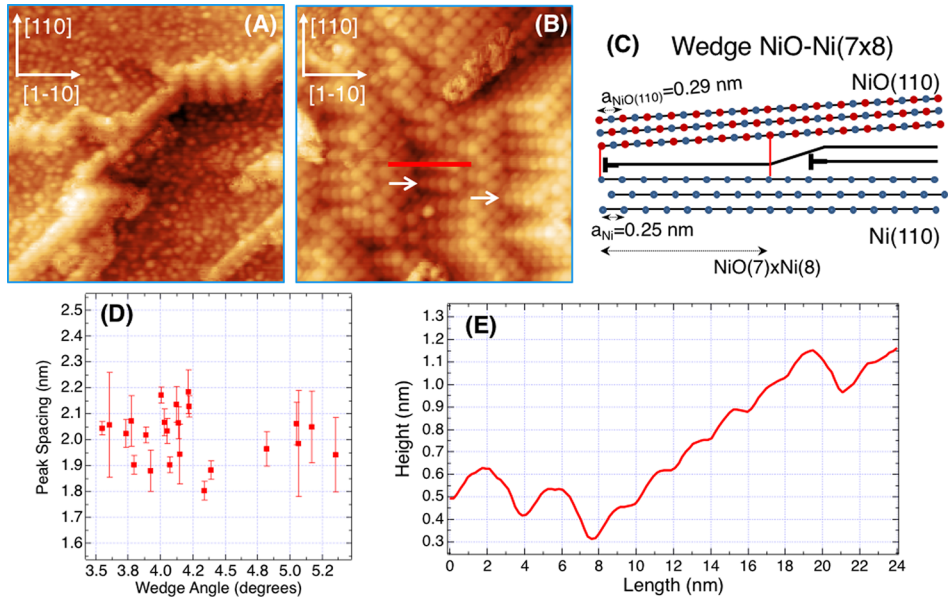

Figure 5. (A, B) Selection of oxide wedges after processing steps E_1 and A_2, respectively, for the Ni−12 wt % Cr(100) sample. The arrow in image B marks secondary wedges, which do not span the entire step edge. (C) Model of the (7 × 8) coincidence wedge structure with the dislocation plane introduced in the underlying substrate to support tilt in each wedge. (D) Summary of the spacing of the intensity maxima in the moiré structures across a large number of wedges from all different experimental steps for the Ni−12 wt % Cr(100) sample. (E) Representative line scan across a wedge marked in image B by a red line. Both images are 50 × 50 nm^2 with 2.0 V and a feedback current of 0.1 nA.

The image inset in Figure 2D shows that parts of the surface have undergone a surface reconstruction, which presents as a distinct cross-type pattern when the empty states are probed using U_{bias} > 2 V. The cross-type reconstruction is the dominant reconstruction among three distinct chemisorbed phases that are seen on the surface but have no exact counterpart in either the pure Ni(100) or Cr(100) surfaces. The analysis of the reconstructions with density functional theory (DFT) calculations has not yet led to a unique assignment and will be pursued in a future publication. We propose that the cross-type reconstruction, which only forms after the second annealing step, is created by transformation or dissolution of the nanoclusters observed in the initial oxidation step. The cross-type reconstruction is reminiscent of ($\sqrt{5}$ × $\sqrt{5}$)$R27°$ bcc Cr(100), but has a unit cell that is twice as large.[37] The cross-type reconstruction might be a surface oxide, or the first layer of $NiCr_2O_4$ or Cr_2O_3, and possibly includes an ordered vacancy structure. It is tentatively interpreted as a surface region with a relatively high Cr-concentration, which is likely important for the nucleation of Cr_2O_3, and injection of Cr-dopants into the NiO layer.[8] Since surface diffusion is significant for oxide growth at this stage, it is very likely that regions with high Cr-concentrations lead to locally doped oxides.[42] The lateral inhomogeneity in the Cr-concentration is hypothesized to play a critical role in connecting surface chemistry and subsequent oxide layer growth.

In addition, the large oxide nodules appear after the second oxidation step (E_2) of Ni−12 wt % Cr(100) and are readily

DOI: 10.1021/acsami.8b15210
ACS Appl. Mater. Interfaces 2018, 10, 43219−43229

apparent in Figure 2D. Their long axis is along the [100] and [010] directions with respect to the Ni−Cr(100) and NiO(100) surfaces. The apparent height of the nodules is extremely sensitive to bias voltage, which is shown in the Supporting Information, section S4.

The NiO coincidence lattice, which figures so prominently in many of the images, is seen in the STM images as moiré patterns with a square symmetry due to cubic crystal structure of Ni and NiO. A detailed view of terrace and wedge (or step edge) NiO is given in Figures 4 and 5. Figure 4 addresses the coincidence lattice on the terrace, and Figure 5 describes the compressed wedge-like coincidence lattice across the step edges. Figure 4 shows the terrace-NiO obtained after a cumulative O_2 exposure of 14 L on the Ni−12 wt % Cr(100) sample and a 500 °C anneal period (step A_2 as classified in Table 1). The peak spacing is on average 2.50 ± 0.02 nm and shows little variation with modulation of U_{bias} (Figure 4A). A representative line profile for U_{bias} = −2.0 V is shown in Figure 4D. Based on the peak spacing a cube-on-cube epitaxial relationship between the Ni−Cr alloy and NiO is confirmed. With a_{Ni} = 0.35 and a_{NiO} = 0.402 nm from the lattice parameter determine by atomic resolution transmission electron microscopy (TEM),[7] a coincidence lattice with the unit NiO−NiCr(6 × 7) yields a period of approximately 2.4 nm. If the generally accepted NiO(100) spacing of 0.417 nm is used, a value of about 2.5 nm is expected and is in even closer agreement with our measured peak spacing of 2.50 ± 0.02 nm. While there is evidence that the NiO(100) grown on dilute Ni−Cr(100) alloys has a lattice spacing of 0.402 nm, the lattice constant of dilute Ni-Cr alloys is nearly identical to that of Ni.[43,44] Given this, a model for the Ni−NiCr(100) coincidence lattice is proposed in Figure 4C. As a side note, the chemisorbed structure (or reconstruction) at the end point of line scan 2 (Figure 4B) shows a square lattice.

The apparent height of the NiO steps between NiO−NiO and NiO−NiCr with chemisorbed oxygen (oxygen-induced reconstruction) is summarized in Figure 4B. The apparent step height NiO−NiO layer is 0.19 ± 0.01 nm and corresponds to the growth of NiO in layers of half unit cells (two atomic layers), and the coincidence lattice signature is conserved for several layers minimizing biaxial strain. Several (6 × 7) unit cells are marked in Figure 4A. and are offset by half a (6 × 7) unit cell across a step edge. On the other hand, the apparent step height measured between the first layer chemisorbed phase on Ni−Cr and NiO depends sensitively on the bias voltage and nearly doubles to reach 0.44 nm at U_{bias} = +4.0 V. At this bias voltage the antibonding p-states of the NiO[15] are probed, while the contributions from the chemisorbed domain are not yet understood. The tunneling current from NiO and the chemisorbed domains do not follow the same bias-voltage dependence, which leads to the strong variation in apparent step height between them. A future DFT calculation of the chemisorbed domains should provide the requisite LDOS and allow for a quantitative interpretation. Figure 6 includes STS spectra from both regions and underscores the differences in the LDOS between them.

Figure 5A,B shows in more detail the NiO at the step edges, which presents as wedgelike structures first reported by Bäumer et al.[28] NiO nucleates first at the step edges and grows subsequently into the top and bottom terraces. The average spacing of the moiré maxima measured along the wedge incline (taken along the [110] and [1$\bar{1}$0] directions) is 2.01 ± 0.07 nm and has an angle of 3.6−5.3° with respect to

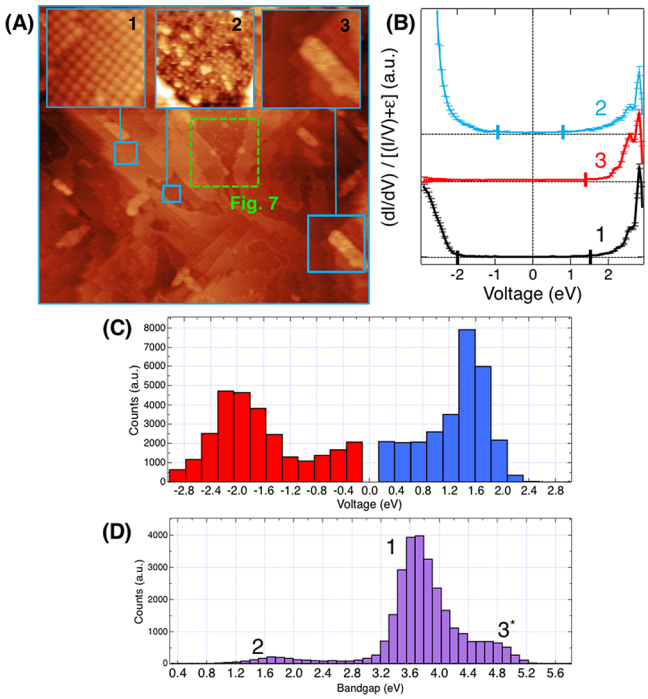

Figure 6. Topography images (A) and band gap and STS spectra (B) for Ni−12 wt % Cr(100) after the 14 L O_2 at 500 °C exposure (step E_2). (A) Large scale image 300 × 300 nm^2 in combination with higher-resolution images of characteristic surface features. From left to right: moiré pattern from the coincidence lattice between Ni(100) and NiO(100), surface reconstruction labeled as "cross-reconstruction" from its visual presentation, and oxide nodule. Images were recorded at 3.0 V and 0.1 nA. The green rectangle marks the region of the band gap and LDOS maps shown in Figure 7. (B) STS spectra for all characteristic regions shown in the high-resolution insets. The spectra are averaged over 20−40 individual spectra extracted from the STS maps recorded in the respective region. (C) This histogram summarizes VBM and CBM positions for all $(dI/dV)/(I/V)$ spectra recorded in the STS map collection for the part A surface area. (D) Histogram of the corresponding band gaps collected for image area of part A, and the labels correspond to the STS spectra (B) and images (A). Note that band gaps larger than 4.2 eV (labeled 3*) are positioned on the nodules and due to suppression of the tunneling current in the valence band, and it is not possible to assess the actual band gap.

the [001] direction (Figures 5D). This reduced periodicity corresponds to a NiO−NiCr(7 × 8) coincidence lattice, where the (110) lattice planes match at the aforementioned coincidence site. The wedge angle is achieved by introducing additional half-planes at the Ni−Cr(100)−NiO interface as shown schematically in Figure 5C, and the geometric structure of the interface stabilizes a narrow range of wedge angles. These sites accommodate NiO formation by creating low-angle grain boundaries at the interface. In addition to the NiO wedge the formation of shorter, secondary wedges is observed, and they are marked by white arrows in Figure 5B. These secondary wedges are a signature of a change in growth mode from Frank−van der Merve to Vollmer−Weber. Luo et al.[6] observed this transition with in situ HRTEM (high-resolution transmission electron microscopy) on Ni−10 atom % Cr at 450 °C, and a similar transition is seen on Cu with a shallow wetting layer of only two atomic layers.[45,46] The Ehrlich−Schwöbel barrier confines Ni-atoms to a single NiO

DOI: 10.1021/acsami.8b15210
ACS Appl. Mater. Interfaces 2018, 10, 43219−43229

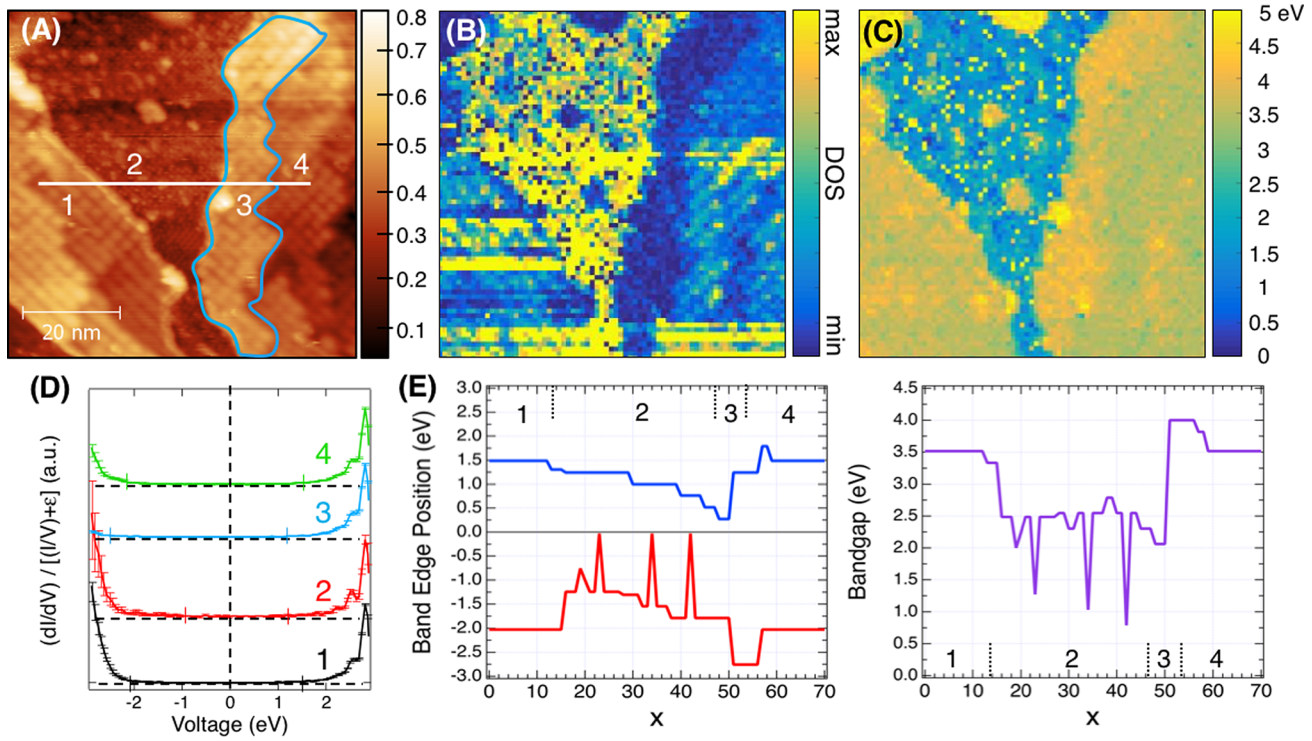

Figure 7. (A) Topography image of the region marked in Figure 6. (B) Corresponding density of states map at $U_{bias} = -2.39$ V. (C) Band gap map. (D) Spectra collected in the characteristic surface regions traversed along the line included in part A. Regions 3 and 4 show identical topography features and band gaps, but present differences in doping. (E) Position of VBM, CBM, and band gap values extracted from all spectra measured across regions 1 to 4 following the white guiding line in part A.

terrace where a new oxide layer nucleates. This results in the formation of stacked oxide islands and a new (110) facet.[7]

The structural heterogeneity observed during the initial stages of oxidation is even more pronounced in the electronic heterogeneity, and can be seen in the LDOS and band gap maps. These maps reflect the LDOS of all surface features, and in addition show inhomogeneous distributions of dopants within a single surface feature. Figures 6 and 7 are used to discuss the electronic structure of the surface after cumulative oxygen exposure of Ni−12 wt % Cr(100) with 14 L O_2 and annealing at 500 °C (E_2 as classified in Table 1). Note that image resolution in the combined STS/STM mode for the topography images is worse than for images recorded exclusively in topography mode. The topography image shown here was captured immediately after the STS map measurement, which allows for unambiguous feature matching.

Figure 6 summarizes characteristic regions, and the STS spectra in Figure 6B are averaged over 20−40 individual spectra recorded within the marked areas in the topography image. Figure 6A. Region 1 corresponds to the NiO moiré pattern; region 2 reflects the cross-type reconstruction, the most prominent surface reconstruction on this sample, and region 3 corresponds to one of the large oxide nodules.

The NiO layer (region 1) has on average a band gap of 3.6 eV, which is lower than the bulk value of 4.3 eV NiO.[47−49] The Fermi level is shifted toward the conduction band minimum (CBM) with respect to the intrinsic Fermi energy position and is commensurate with n-type doping. The reconstructed region 2 has a smaller band gap, and the band edges are positioned at −1.0 and 0.9 eV, respectively. The shallower slope at the band edges is likely due to additional states specific for this reconstruction. The STS spectrum of the large oxide nodules in region 3 shows a very small intensity for the valence band, which prevents a reliable determination of a band gap.[50] The $(dI/dV)/(I/V)$ values for the valence band show the reduction in the transmission function due to the insulating nature of the oxide nodule. The very low $(dI/dV)/(I/V)$ is also reflected in bias dependent topography images included in the Supporting Information, section S4. Figure 6C,D summarizes all values for the valence band maxima (VBM) and conduction band minima (CBM), as well as band gap values, respectively, for the entire image area of Figure 6A. NiO dominates the surface and the position of the maxima for VBM, and CBM histograms reflect the n-type doping we observed in the individual spectra. The most-probable band gap value of 3.6 eV is attributed to the NiO layers; larger values correspond to oxide nodules, and values centered around 1.7 eV represent the chemisorbed regions.

To understand the heterogeneous electronic structure of the Ni−12 wt % Cr(100) surface after oxidation, a section of Figure 6A was selected that represented the spatial variation of the distinct surface oxide features. Figure 7 addresses the area marked with a green rectangle in Figure 6, and the image of this region is shown in Figure 7A. Figure 7B includes the LDOS map—a cut through all spectra at $U_{bias} = -2.39$ V, and the corresponding $(dI/dV)/(I/V)$ value is displayed as a function of position. Figure 7C shows the band gap map for the same area. A few regions in the LDOS map have some streaks due to tip changes during measurement and are excluded from the discussion. The individual spectra in Figure 7D correspond to different segments along the line in the STM image, which crosses from the NiO region (1) onto the chemisorbed surface (2), and back onto a section of NiO, which is divided into segments 3 and 4. The band gap and

DOI: 10.1021/acsami.8b15210
ACS Appl. Mater. Interfaces 2018, 10, 43219−43229

band edge positions are summarized in Figure 7E, and the different line segments are marked. The standard deviation for VBM (CBM) values is 0.2 eV (0.08 eV) for segments 1 and 4, 0.4 eV for VBM and CBM in segment 2, and 0.18 eV (VBM) and 0.16 (CBM) for segment 3. The standard deviation was calculated for data sets consisting of ±4 STS pixels around each data point positioned on the line and reflects the experimental variability. Segment 2 is relatively inhomogeneous and shows significant local variations in its LDOS due to some very small clusters embedded in the cross-type reconstruction. Segments 1 and 4 are very similar in terms of band gap, VBM, and CBM values, and are both slightly n-doped. Note that the NiO section left of segment 1 shows the identical band gap value and LDOS.

Segments 3 and 4 are particularly interesting: the band gap is slightly larger in segment 3, and the position of the Fermi energy is shifted closer to the CBM indicating a stronger doping compared to NiO segment 4, and segment 1. NiO segment 3 is marked with a blue outline in the topography image, and the corresponding region can clearly be identified in the LDOS map. Candidates for oxide doping are defects such as trivalent, substitutional Cr^{3+}, which increases the vacancy concentration and hence reduces the hole concentration.[42] The vacancies created by introduction of Cr^{3+} also provide a mechanism for the accelerated growth of NiO.[8] Additional gap states can arise from local O-deficiencies, or the presence of solute trapped Cr^{2+}, and Cr^{3+}, which has recently been reported.[42,51] The overall position of the Fermi energy within the gap is determined by the entirety of the defect and dopant inventory and cannot be attributed to one specific, dominant gap state at present. As a consequence, the assumption of a homogeneous electric field at the interface between alloys and oxide, which is commonly made in Cabrera−Mott growth models, should be revisited.

DISCUSSION

The comparison between Ni(100) and Ni−Cr(100) oxidation demonstrates the significant changes in the formation of surface oxides caused by alloying even with relatively small amounts of Cr. NiO dominates the surface oxide during the early stages of oxidation, which is in agreement with the literature in the temperature regime of the present study.[6,7,11,52,8,52] The impact of Cr on NiO nucleation, and the wide range of surface features that emerge early in the oxidation process, illustrates the complexity of alloy surface chemistry. Consideration must be given to the preferred nucleation and growth site for each constituent metal in the alloy and their corresponding oxide phase, and the effects of the oxide growth on surrounding phases.

Introduction of Cr significantly enhances NiO nucleation and growth, but also contributes to the emergence of additional oxide features including novel reconstructions and large oxide nodules not seen during the oxidation of Ni(100). Recent work has shown that substituting Cr for a Ni surface atom enhances the affinity for bonding between oxygen and Ni−Cr surfaces,[53,54] underscoring the role of Cr in promoting NiO formation. The enhanced NiO nucleation goes hand in hand with accelerated NiO growth, which is aided by Cr-doping. We propose two mechanisms for the enhanced NiO nucleation: (i) Cr segregates to the step edges and facilitates oxide nucleation by changing the reaction kinetics and local activation barriers, or (ii) Cr prevents reconstruction-induced step faceting by lowering step edge atom mobility; kink sites for nucleation are therefore retained. This question can be resolved in future work by targeting very low oxygen exposures and lower Cr-concentration alloys in conjunction with DFT calculations to assess the most likely Cr-position in the alloy surface.

The oxidation of Ni−Cr leads also to structural and compositional changes in the alloy surface itself and includes (i) faceting of step edges by NiO growth, which is driven by the epitaxial relationship between the Ni−Cr and NiO lattices, and (ii) the emergence of presumably Cr-rich regions within a novel cross-type reconstruction. The characteristic symmetry of the cross-type reconstruction has no counterpart in the fcc Ni(100) surfaces and is reminiscent of the oxygen-induced bcc Cr(100)[33,37] reconstructions. This led us to propose a Cr-rich surface region formed by lateral segregation of Cr. Consequently, we cannot think about the Ni−Cr alloy surfaces as a homogeneous system with a random distribution of Cr-atoms but should revise this picture to include lateral element segregation. The effect of this segregation on local oxidation reactions should also be considered in greater detail. One of the consequences of local variations in Cr-concentrations beyond the atomic-length scale of a solid solution is heterogeneity in oxide doping, which is likely the reason for the variations in electronic structure seen in Figures 6 and 7. The assumption of uniform oxide coverage is inadequate within the pre-Cabrera−Mott regime. As such, the description of the surface electronic structure and compositional variation can account for the heterogeneity observed and will be important for future work.

CONCLUSIONS

The surface reactions of binary Ni−Cr alloys were studied by nanoscale characterization of the geometric and electronic structure. The combination of STM and STS maps enabled us to deepen our understanding of the structural, compositional, and electronic heterogeneity that emerges in the initial stages of the oxidation process. Some aspects of the oxidation, which are controlled by geometric constraints and include the coincidence lattices formed by NiO at the step edges and on the terraces, have direct counterparts in the oxidation of Ni(100) surfaces. However, surface processes controlled by local chemistry and kinetics, such as reconstruction-driven step edge faceting, lateral segregation of Cr, and the formation of new reconstructions, are uniquely changed by the addition of small amounts of Cr. The electronic heterogeneity is likely impactful for the continuation of NiO growth and is coupled to established mechanisms of NiO accelerated growth via Cr-dopant-induced vacancies. The pre-Cabrera−Mott regime sets the stage for the transition to Cabrera−Mott and field controlled oxide growth, and the next step in this work is to understand this transition. It is particularly important to establish which features of pre-Cabrera−Mott heterogeneity have an impact on the continued oxide growth and passive film performance.

ASSOCIATED CONTENT

Supporting Information

The Supporting Information is available free of charge on the ACS Publications website at DOI: 10.1021/acsami.8b15210.

Additional descriptions and figures including STS curves, VBM and CBM distributions, band gaps, STM images, step heights, and an illustration (PDF)

DOI: 10.1021/acsami.8b15210
ACS Appl. Mater. Interfaces 2018, 10, 43219−43229

AUTHOR INFORMATION

Corresponding Author

*E-mail: pr6e@virginia.edu.

ORCID

William H. Blades: 0000-0002-0665-7981

Petra Reinke: 0000-0002-4544-5906

Notes

The authors declare no competing financial interest.

ACKNOWLEDGMENTS

This work is supported by the Office of Naval Research MURI "Understanding Corrosion in Four Dimensions," Grant N00014-14-1-0675, under program manager Dr. David Shifler.

REFERENCES

(1) Atkinson, A. Transport Processes during the Growth of Oxide Films at Elevated Temperature. *Rev. Mod. Phys.* **1985**, *57* (2), 437−470.

(2) Wood, G. C.; Chattopadhyay, B. Transient Oxidation of Ni-Base Alloys. *Corros. Sci.* **1970**, *10* (7), 471−480.

(3) Chattopadhyay, B.; Wood, G. C. The Transient Oxidation of Alloys. *Oxid. Met.* **1970**, *2* (4), 373−399.

(4) De Los Santos Valladares, L.; Ionescu, A.; Holmes, S.; Barnes, C. H. W.; Bustamante Domínguez, A.; Avalos Quispe, O.; González, J. C.; Milana, S.; Barbone, M.; Ferrari, A. C.; et al. Characterization of Ni Thin Films Following Thermal Oxidation in Air. *J. Vac. Sci. Technol., B: Nanotechnol. Microelectron.: Mater., Process., Meas., Phenom.* **2014**, *32* (5), 051808.

(5) Mohanty, P.; Rath, C.; Mallick, P.; Biswal, R.; Mishra, N. C. UV−Visible Studies of Nickel Oxide Thin Film Grown by Thermal Oxidation of Nickel. *Phys. B* **2010**, *405* (12), 2711−2714.

(6) Luo, L.; Zou, L.; Schreiber, D. K.; Baer, D. R.; Bruemmer, S. M.; Zhou, G.; Wang, C.-M. In-Situ Transmission Electron Microscopy Study of Surface Oxidation for Ni−10Cr and Ni−20Cr Alloys. *Scr. Mater.* **2016**, *114*, 129−132.

(7) Luo, L.; Zou, L.; Schreiber, D. K.; Olszta, M. J.; Baer, D. R.; Bruemmer, S. M.; Zhou, G.; Wang, C.-M. In Situ Atomic Scale Visualization of Surface Kinetics Driven Dynamics of Oxide Growth on a Ni−Cr Surface. *Chem. Commun.* **2016**, *52* (16), 3300−3303.

(8) Unutulmazsoy, Y.; Merkle, R.; Fischer, D.; Mannhart, J.; Maier, J. The Oxidation Kinetics of Thin Nickel Films between 250 and 500 °C. *Phys. Chem. Chem. Phys.* **2017**, *19* (13), 9045−9052.

(9) Lutton, K.; Gusieva, K.; Ott, N.; Birbilis, N.; Scully, J. R. Understanding Multi-Element Alloy Passivation in Acidic Solutions Using Operando Methods. *Electrochem. Commun.* **2017**, *80*, 44−47.

(10) Sprowl, L. H.; Adam, B. M.; Tucker, J. D.; Árnadóttir, L. First-Principles Study of the Products of CO2 Dissociation on Nickel-Based Alloys: Trends in Energetics with Alloying Element. *Surf. Sci.* **2018**, *677*, 219.

(11) Ramanathan, R.; Ramalingam, G.; Perepezko, J. H.; Reinke, P.; Voorhees, P. W. Evolution of NiO Island Size Distributions During the Oxidation of a Ni-5Cr Alloy: Experiment and Modeling. *ACS Appl. Mater. Interfaces* **2018**, *10*, 9136.

(12) Gusieva, K.; Cwalina, K. L.; Blades, W. H.; Ramalingam, G.; Perepezko, J. H.; Reinke, P.; Scully, J. R. Repassivation Behavior of Individual Grain Facets on Dilute Ni−Cr and Ni−Cr−Mo Alloys in Acidified Chloride Solution. *J. Phys. Chem. C* **2018**, *122* (34), 19499−19513.

(13) Bertrams, T.; Neddermeyer, H. Growth of NiO(100) Layers on Ag(100): Characterization by Scanning Tunneling Microscopy. *J. Vac. Sci. Technol., B: Microelectron. Process. Phenom.* **1996**, *14* (2), 1141−1144.

(14) Schintke, S.; Schneider, W.-D. Insulators at the Ultrathin Limit: Electronic Structure Studied by Scanning Tunnelling Microscopy and Scanning Tunnelling Spectroscopy. *J. Phys.: Condens. Matter* **2004**, *16* (4), R49.

(15) Castell, M. R.; Wincott, P. L.; Condon, N. G.; Muggelberg, C.; Thornton, G.; Dudarev, S. L.; Sutton, A. P.; Briggs, G. A. D. Atomic-Resolution STM of a System with Strongly Correlated Electrons:NiO(001) Surface Structure and Defect Sites. *Phys. Rev. B: Condens. Matter Mater. Phys.* **1997**, *55* (12), 7859−7863.

(16) Cabrera, N. *Rep. Prog. Phys.* **1949**, *12*, 163−184.

(17) Wagner, C. Equations for Transport in Solid Oxides and Sulfides of Transition Metals. *Prog. Solid State Chem.* **1975**, *10*, 3−16.

(18) Seyeux, A.; Maurice, V.; Marcus, P. Oxide Film Growth Kinetics on Metals and Alloys: I. Physical Model. *J. Electrochem. Soc.* **2013**, *160* (6), C189−C196.

(19) Lankhorst, M. H. R.; Bouwmeester, H. J. M.; Verweij, H. Thermodynamics and Transport of Ionic and Electronic Defects in Crystalline Oxides. *J. Am. Ceram. Soc.* **1997**, *80* (9), 2175−2198.

(20) Haugsrud, R. On the High-Temperature Oxidation of Nickel. *Corros. Sci.* **2003**, *45* (1), 211−235.

(21) Holloway, P. H.; Hudson, J. B. Kinetics of the Reaction of Oxygen with Clean Nickel Single Crystal Surfaces: I. Ni(100) Surface. *Surf. Sci.* **1974**, *43* (1), 123−140.

(22) Steffen, J.; Hofmann, S. Oxidation of NiCr and NiCrFe Alloys at Room Temperature. *Surf. Interface Anal.* **1988**, *11* (12), 617−626.

(23) Jeng, S.-P.; Holloway, P. H.; Batich, C. D. Surface Passivation of Ni/Cr Alloy at Room Temperature. *Surf. Sci.* **1990**, *227* (3), 278−290.

(24) Hoflund, G. B.; Epling, W. S. Oxidation Study of a Polycrystalline Ni/Cr Alloy I: Room-Temperature Exposure to O2. *Thin Solid Films* **1997**, *307* (1), 126−132.

(25) Marcus, P.; Maurice, V. Atomic Level Characterization in Corrosion Studies. *Philos. Trans. R. Soc., A* **2017**, *375*, 20160414.

(26) Calvarin, G.; Molins, R.; Huntz, A. M. *Oxid. Met.* **2000**, *53*, 25−48.

(27) Kopatzki, E.; Behm, R. J. Step Faceting: Origin of the Temperature Dependent Induction Period in Ni(100) Oxidation. *Phys. Rev. Lett.* **1995**, *74* (8), 1399−1402.

(28) Bäumer, M.; Cappus, D.; Kuhlenbeck, H.; Freund, H.-J.; Wilhelmi, G.; Brodde, A.; Neddermeye, H. The Structure of Thin NiO(100) Films Grown on Ni(100) as Determined by Low-Energy-Electron Diffraction and Scanning Tunneling Microscopy. *Surf. Sci.* **1991**, *253* (1), 116−128.

(29) Smeenk, R. G.; Tromp, R. M.; Frenken, J. W. M.; Saris, F. W. The Oxidation of Ni(100) Studied by Medium Energy Ion Scattering. *Surf. Sci.* **1981**, *112* (3), 261−271.

(30) Kopatzki, E.; Behm, R. J. STM Imaging and Local Order of Oxygen Adlayers on Ni(100). *Surf. Sci.* **1991**, *245* (3), 255−262.

(31) Stuckless, J. T.; Wartnaby, C. E.; Al-Sarraf, N.; Dixon-Warren, S. J. B.; Kovar, M.; King, D. A. Oxygen Chemisorption and Oxide Film Growth on Ni{100}, {110}, and {111}: Sticking Probabilities and Microcalorimetric Adsorption Heats. *J. Chem. Phys.* **1997**, *106* (5), 2012−2030.

(32) Norton, P. R.; Tapping, R. L.; Goodale, J. W. A Photoemission Study of the Interaction of Ni(100), (110) and (111) Surfaces with Oxygen. *Surf. Sci.* **1977**, *65* (1), 13−36.

(33) Foord, J. S.; Lambert, R. M. Oxygen Chemisorption and Corrosion on Cr(100) and Cr(110) Single Crystal Surfaces. *Surf. Sci.* **1985**, *161* (2), 513−520.

(34) Hope, G. A.; Ritchie, I. M. The Oxidation of Thin Chromium Films. *Thin Solid Films* **1976**, *34* (1), 111−114.

(35) Salomonsen, G.; Norman, N.; Lonsjo, O.; Finstad, T. G. Kinetics and Mechanism of Oxide Formation on Cr Thin Films. *J. Phys.: Condens. Matter* **1989**, *1* (42), 7843.

(36) Peter, R.; Saric, I.; Piltaver, I. K.; Badovinac, I. J.; Petravic, M. Oxide Formation on Chromium Metal Surfaces by Low-Energy Oxygen Implantation at Room Temperature. *Thin Solid Films* **2017**, *636*, 225−231.

(37) Schmid, M.; Leonardelli, G.; Sporn, M.; Platzgummer, E.; Hebenstreit, W.; Pinczolits, M.; Varga, P. Oxygen-Induced Vacancy Formation on a Metal Surface. *Phys. Rev. Lett.* **1999**, *82* (2), 355−358.

DOI: 10.1021/acsami.8b15210
ACS Appl. Mater. Interfaces 2018, 10, 43219−43229

(38) Ramalingam, G.; Reinke, P. Growth of Ni and Ni-Cr Alloy Thin Films on MgO(001): Effect of Alloy Composition on Surface Morphology. *J. Appl. Phys.* **2016**, *120* (22), 225302.
(39) Feenstra, R. M. Tunneling Spectroscopy of the (110) Surface of Direct-Gap III-V Semiconductors. *Phys. Rev. B: Condens. Matter Mater. Phys.* **1994**, *50* (7), 4561−4570.
(40) Feenstra, R. M.; Stroscio, J. A.; Fein, A. P. Tunneling Spectroscopy of the Si(111)2 × 1 Surface. *Surf. Sci.* **1987**, *181* (1), 295−306.
(41) Cahn, J. W.; Handwerker, C. A. Equilibrium Geometries of Anisotropic Surfaces and Interfaces. *Mater. Sci. Eng., A* **1993**, *162* (1), 83−95.
(42) Yu, X.; Gulec, A.; Sherman, Q.; Cwalina, K. L.; Scully, J. R.; Perepezko, J. H.; Voorhees, P. W.; Marks, L. D. Nonequilibrium Solute Capture in Passivating Oxide Films. *Phys. Rev. Lett.* **2018**, *121* (14), 145701.
(43) Karmazin, L. Lattice Parameter Studies of Structure Changes of L ∼ i-Cr Alloys in the Region of Ni2Cr. *Mater. Sci. Eng.* **1982**, *54*, 247−256.
(44) Chen, J. K.; Farkas, D.; Reynolds, W. T. Atomistic Simulation of an f.c.c./b.c.c. Interface in Ni—Cr Alloys. *Acta Mater.* **1997**, *45* (11), 4415−4421.
(45) Zhou, G.; Luo, L.; Li, L.; Ciston, J.; Stach, E. A.; Saidi, W. A.; Yang, J. C. In Situ Atomic-Scale Visualization of Oxide Islanding during Oxidation of Cu Surfaces. *Chem. Commun.* **2013**, *49* (92), 10862−10864.
(46) Li, L.; Luo, L.; Ciston, J.; Saidi, W. A.; Stach, E. A.; Yang, J. C.; Zhou, G. Surface-Step-Induced Oscillatory Oxide Growth. *Phys. Rev. Lett.* **2014**, *113* (13), 136104.
(47) Sawatzky, G. A.; Allen, J. W. Magnitude and Origin of the Band Gap in NiO. *Phys. Rev. Lett.* **1984**, *53* (24), 2339−2342.
(48) Schintke, S.; Schneider, W.-D. Insulators at the Ultrathin Limit: Electronic Structure Studied by Scanning Tunnelling Microscopy and Scanning Tunnelling Spectroscopy. *J. Phys.: Condens. Matter* **2004**, *16* (4), R49.
(49) Schintke, S.; Messerli, S.; Pivetta, M.; Patthey, F.; Libioulle, L.; Stengel, M.; De Vita, A.; Schneider, W.-D. Insulator at the Ultrathin Limit: MgO on Ag(001). *Phys. Rev. Lett.* **2001**, *87* (27), 276801.
(50) Sommerhalter, C.; Matthes, T. W.; Boneberg, J.; Leiderer, P.; Lux-Steiner, M. C. Tunneling Spectroscopy on Semiconductors with a Low Surface State Density. *J. Vac. Sci. Technol., B: Microelectron. Process. Phenom.* **1997**, *15* (6), 1876−1883.
(51) Latu-Romain, L.; Parsa, Y.; Mathieu, S.; Vilasi, M.; Galerie, A.; Wouters, Y. Towards the Growth of Stoichiometric Chromia on Pure Chromium by the Control of Temperature and Oxygen Partial Pressure. *Corros. Sci.* **2017**, *126*, 238−246.
(52) Jeng, S.-P.; Holloway, P. H.; Asbury, D. A.; Hoflund, G. B. Changes Induced at Ni/Cr Alloy Surfaces by Annealing and Oxygen Exposure. *Surf. Sci.* **1990**, *235* (2), 175−185.
(53) Samin, A. J.; Taylor, C. D. First-Principles Investigation of Surface Properties and Adsorption of Oxygen on Ni-22Cr and the Role of Molybdenum. *Corros. Sci.* **2018**, *134*, 103−111.
(54) Sprowl, L. H.; Adam, B. M.; Tucker, J. D.; Árnadóttir, L. First-Principles Study of the Products of CO2 Dissociation on Nickel-Based Alloys: Trends in Energetics with Alloying Element. *Surf. Sci.* **2018**, *677*, 219−231.

DOI: 10.1021/acsami.8b15210
ACS Appl. Mater. Interfaces 2018, 10, 43219−43229